Catalysis Science & Technology

PAPER

View Article Online
View Journal | View Issue

Cite this: *Catal. Sci. Technol.*, 2016, **6**, 7841

Effect of carbon supports on RhRe bifunctional catalysts for selective hydrogenolysis of tetrahydropyran-2-methanol†

Pranav U. Karanjkar,[a] Samuel P. Burt,[a] Xiaoli Chen,[ab] Kevin J. Barnett,[a] Madelyn R. Ball,[a] Mrunmayi D. Kumbhalkar,[a] Xiaohong Wang,[b] James B. Miller,[a] Ive Hermans,[ac] James A. Dumesic[a] and George W. Huber*[a]

Tetrahydropyran-2-methanol undergoes selective C–O–C hydrogenolysis to produce 1,6-hexanediol using a bifunctional RhRe (reducible metal with an oxophilic promoter) catalyst supported on Vulcan XC-72 carbon (VXC) with >90% selectivity. This RhRe/VXC catalyst is stable over 40 h of reaction in a continuous flow fixed bed reactor. The hydrogenolysis activity of RhRe/VXC is two orders-of-magnitude higher than that of RhRe supported on Norit Darco 12X40 activated carbon (NDC). STEM–EDS analysis reveals that, compared to the RhRe/VXC catalyst, the Re and Rh component metals are segregated on the surface of the low activity RhRe/NDC catalyst, suggesting that Rh and Re in close proximity ("bimetallic" particles) are required for an active hydrogenolysis catalyst. Differences in metal distribution on the carbon surfaces are, in turn, linked to the properties of the carbons: NDC has both a higher surface area and surface oxygen content. The low areal density of Rh and Re precursors on the high area NDC and/or interactions of the precursors with its O functional groups may interfere with the formation of the bimetallic species required for an active catalyst.

Received 17th August 2016,
Accepted 9th September 2016

DOI: 10.1039/c6cy01763k

www.rsc.org/catalysis

1. Introduction

Supported bimetallic catalysts containing a reducible metal and an oxophilic promoter have been studied for selective C–O cleavage reactions in biomass conversion.[1–4] Carbon-supported bifunctional catalysts have been used extensively for selective hydrogenolysis of cyclic ethers and other C–O–C linkages.[4–6] For example, Chia *et al.* reported that a Re promoted Rh/C catalyst is selective for the hydrogenolysis of C–O bonds found in a broad range of cyclic ethers and polyols.[4] Daniel *et al.* observed that the activity of a PtRe/C catalyst for glycerol hydrogenolysis was an order-of-magnitude higher than that of monometallic Pt/C.[7] Selective hydrogenolysis of tetrahydropyran-2-methanol (THP-2M) to 1,6-hexanediol (1,6-HDO) with >90% selectivity using Re promoted Rh catalysts has also been reported.[4,5,8] The synergy between the reducible metal Rh and the oxophilic promoter Re is important for the selectivity to 1,6-HDO in this reaction.[4,5,8] C–O hydrogenolysis over RhRe/C has been proposed to occur through a bifunctional mechanism involving acid-catalyzed ring-opening at the Re promoter followed by metal-catalyzed hydrogenation at a nearby Rh.[5,9] Multiple studies from different researchers have shown that neither Rh nor Re alone is effective for hydrogenolysis of THP-2M.[4–12]

Various allotropic varieties of carbon, including active carbons and carbon blacks, have long been used as catalyst supports.[13,14] For aqueous phase biomass processing reactions, carbon supports are used because of their high surface area (200–2000 m^2 g^{-1}) and hydrothermal stability.[15–18] Both the physical properties and surface chemistry of carbon supports can affect the properties of the supported active catalytic phase; carbon surfaces have, therefore, often been functionalized by thermal or chemical post-treatments to increase the surface area or create specific functionalities.[19–22] For example, Figueiredi *et al.* showed that gas phase oxidation of activated carbon at 698 K for 20 h increases the concentration of oxygen-containing functional groups by >100%. Surface functional groups, such as –OH and –COOH, can anchor the metal precursor to the carbon, thus restricting the metal's surface mobility.[23] However, even when surface chemistry is held constant, differences in carbon morphology can influence the properties of supported metal nanoparticles. For example, Cabiac *et al.* reported that Pd catalysts supported by activated carbons of different surface areas and pore volumes, but with similar concentrations of surface functional

---

[a] *Department of Chemical and Biological Engineering, University of Wisconsin-Madison, USA. E-mail: gwhuber@wisc.edu*
[b] *Department of Chemistry, Key Lab of Polyoxometalate Science of Ministry of Education, Northeast Normal University, China*
[c] *Department of Chemistry, University of Wisconsin-Madison, USA*

† Electronic supplementary information (ESI) available. See DOI: 10.1039/c6cy01763k

groups, can have Pd particle sizes that vary from 2.8 nm to 8.5 nm.[24]

Little attention has been given to how the physical and chemical characteristics of carbons affect the structural evolution and catalytic activity of bimetallic particles that they support. In this study, we compare the performances of well characterized bifunctional RhRe catalysts supported on two very different carbon supports, Norit Darco 12X40 (NDC by Cabot Corp., an activated carbon) and Vulcan XC-72 (VXC by Cabot Corp., a carbon black).

2. Experimental

2.1. Catalyst preparation

Single and bimetallic catalysts were prepared by incipient wetness impregnation of the carbon supports with aqueous solutions of $RhCl_3 \cdot xH_2O$ (Sigma-Aldrich) and NH_4ReO_4 (Sigma-Aldrich). The RhRe catalysts were obtained by successive impregnation of dried, unreduced Rh/C with an aqueous solution of NH_4ReO_4 (0.12 M). Because of NDC's lower incipient wetness point, the NH_4ReO_4 solution was impregnated in two stages with air-drying of the catalyst at 383 K in-between. All RhRe catalysts examined in this work contained 4 wt% Rh with an atomic ratio of Rh : Re = 1.0 : 0.5. Before use in experiments, the catalysts were dried in air at 383 K, reduced in flowing hydrogen at 723 K (unless noted otherwise), and passivated with flowing 1 vol% O_2 in He at room temperature. This reduction and passivation was considered the last step of catalyst synthesis. Monometallic Re/NDC and Re/VXC with 3.6 wt% Re were prepared by incipient wetness impregnation for use in X-ray absorption spectroscopy studies.

2.2. Catalyst activity studies

2.2.1. Continuous flow fixed bed reactor. Hydrogenolysis of THP-2M was conducted in a stainless-steel tubular flow reactor (30 cm long, 6.35 mm outer diameter), arranged in an upflow configuration and heated by using a tube furnace (Thermcraft Inc. No. 114-12-1ZH). A uniform temperature profile along the catalyst bed was achieved by placing an aluminum filler in the void between the furnace wall and the reactor tube. One gram of the RhRe/VXC catalyst, without a diluent, was loaded into the reactor with quartz wool and quartz beads packed on both sides. Before the reaction, the catalyst was reduced *in situ* under a H_2 flow (100 mL min^{-1}) at 473 K for 15 min. After reduction, the reactor was cooled to the desired reaction temperature and pressurized to 40 bar H_2. An aqueous 5 wt% THP-2M solution was fed to the reactor using an Agilent Prostar HPLC pump with co-fed H_2 (40 mL min^{-1}). A stainless steel gas–liquid separator (300 mL) was used to accumulate liquid products at the reactor outlet. The accumulated liquid product was drained periodically into a collector container, filtered through a 0.22 μm PES syringe filter and then analyzed by HPLC and GC (see section 2.2.3 for details). The gaseous products continued to flow through a back pressure regulator to maintain the reaction pressure. Both an excess flow shut-off valve and a pressure relief valve were also installed in the reactor system to ensure safe operation.

2.2.2. Batch reactor. Reactions using a 25 mL reaction mixture volume were performed in a 50 mL pressure vessel (Hastealloy C-276, model 4792, Parr Instrument) inside a parallel, automated reactor system (HEL group). A fixed amount of catalyst (0.175 g) was loaded into the reaction vessel. Before introduction of the reactant, the reactor was purged with He and then H_2, and pressurized to 40 bar with H_2. The catalyst was reduced at 473 K in H_2 for 15 min, and then cooled to room temperature. A 25 ml reactant solution of 5 wt% THP-2M (Sigma-Aldrich, 98% purity) in HPLC water was injected into the reactor using an HPLC pump. After pumping the feed solution into the reactor, the reactor pressure was readjusted to 40 bar H_2. The reaction was conducted at 393 K with continuous magnetic stirring at 500 rpm. After reaction, the product mixture was filtered through a 0.22 μm polyethersulfone (PES) syringe filter (Restek #23966) for quantitative analysis by HPLC and GC (see section 2.2.3 for details). To obtain temporal concentration profiles over the course of reaction, a 100 mL pressure vessel (Hastealloy C-276, model 4560, Parr Instrument Company) was used to conduct reactions with a 50 mL initial reaction volume. The catalyst pre-reduction process was the same as that used for the 25 mL reaction. The reaction temperature was controlled at 393 K along with the stirring speed using a Parr 4848 controller. Samples (about 1 mL) were periodically withdrawn from the reactor through a dip tube. The reactor was repressurized after withdrawing each sample. The samples were immediately quenched in an ice water bath and filtered through a 0.22 μm PES syringe filter before analysis by HPLC and GC.

2.2.3. Product analysis. The feed solutions and the liquid products from both the batch and continuous flow reactors were analyzed using a high-performance liquid chromatograph (HPLC; Shimadzu, LC-20AT) equipped with a refractive index (RID-10 A) detector. Separation was achieved using a Biorad Aminex HPX-87H column at 303 K with 5 mM H_2SO_4 as the mobile phase flowing at a rate of 0.6 mL min^{-1}. For each analysis, the injection volume was 1 μL. HPLC analysis was used to quantify concentrations of THP-2M, 1,6-HDO and its isomers. To quantify some of the other by-products (including 1-hexanol, 2MTHP, and 1-pentanol), the liquid products were also analyzed using a gas chromatograph (Shimadzu, GC-2010) equipped with a flame ionization detector (FID) and a Restek RTX-VMS capillary column. The column flow rate was 0.43 mL min^{-1} with a He carrier gas. The GC oven temperature was initially held at 313 K for 5 min, ramped to 513 K at 7.5 K min^{-1}, and kept at 513 K for 15 min. The gas effluent from the continuous flow reactor was analyzed using a gas chromatograph (Shimadzu, GC-2014) equipped with an FID and a Restek RT-Q-Bond capillary column as well as a thermal conductivity detector and a ShinCarbon ST micropacked column. The GC oven temperature was initially held at 308 K for 5 min, ramped to 423 K at 5 K min^{-1}, and kept at 423 K for 15 min. The reaction products were also analyzed by ICP for leaching of the Rh and Re components of the catalyst. No leaching of Rh or Re was observed for all experiments reported in this study.

2.3. Catalyst characterization

2.3.1. CO chemisorption. Carbon monoxide chemisorption studies were carried out using an AutoChem II 2920 system (Micromeritics). Prior to the CO uptake measurements, the catalysts were reduced using the pre-reaction protocol. After reduction, the catalyst was flushed with He for 90 min at 473 K to remove the adsorbed hydrogen. The CO-pulse chemisorption was performed at 323 K using 10 vol% CO in He (Airgas).

2.3.2. Inductively coupled plasma–atomic emission spectroscopy (ICP–AES). Bulk elemental compositions of the catalysts were determined in inductively coupled plasma (ICP) experiments using a Perkin Elmer 2000 ICP-AES. Samples were first digested in *aqua regia* and then diluted in 18 MΩ water to target Rh and Re concentrations of approximately 5 ppm for analysis. To determine the amount of Re that may have leached from the catalyst into the reaction mixture, liquid products from the reaction were analyzed using a Plasma 400 ICP emission spectrometer (Perkin-Elmer).

2.3.3. Surface area characterization. The BET surface areas of the carbon supports were determined from N_2 adsorption isotherms obtained at 77 K using an ASAP 2020 system (Micromeritics). The carbon samples were degassed under vacuum (<0.07 mmHg) at 573 K for 2 h prior to analysis. The micropore surface area of the carbon samples was calculated from a *t*-plot using the N_2 isotherm. Water adsorption experiments were performed using a 3Flex instrument (Micromeritics) at 298 K. Water was purified by three freeze-and-thaw cycles and the carbon samples were degassed under vacuum (<0.07 mmHg) at 383 K for 12 h prior to analysis. The water uptake was determined at the relative pressure (P/P_o) that showed complete filling of the pores in the N_2 adsorption.

2.3.4. X-ray photoelectron spectroscopy (XPS). The surface compositions of the carbon supports were characterized by XPS using a K-alpha XPS (Thermo Scientific) instrument with a micro-focused monochromatic Al K_α X-ray source. The carbons were not pretreated prior to the measurements, because they are not pretreated prior to catalyst synthesis. The samples were analyzed at 10^{-7} mbar pressure and room temperature. The spectra in the C 1s, O 1s, S 2p, Si 2p, Al 2p, and Na 1s regions were collected over multiple scans; the number of scans was adjusted for each element (C = 10, O = 150, S = 120, Si = 75, Al = 175, Na = 150) to obtain an acceptable signal/noise ratio. The pass energy was held at 50 eV, the dwell time at 50 ms, and the energy step size at 0.2 eV for each region. Each region was integrated using the Avantage (Thermo Scientific) software package for determination of surface composition.

2.3.5. Diffuse reflectance infrared Fourier transform spectroscopy (DRIFTS). The DRIFTS spectra of the carbon supports were acquired in a N_2 atmosphere at room temperature using a Bruker Alpha FT-IR spectrometer. The carbon samples were not pretreated prior to the measurements, because they are not pretreated prior to catalyst synthesis. The samples were diluted in KBr in a mass ratio of approximately 1 : 50 (C : KBr). Background spectra were acquired on an empty Cu plate. The background and sample measurements used a resolution of 4 cm^{-1} and 100 scans. The spectra were deconvoluted and integrated using the Fityk software package; the spectral features were assigned to specific functional groups based on literature reports.[23,25–27]

2.3.6. X-ray absorption spectroscopy (XAS). XAS was performed at the Advanced Photon Source (APS) at Argonne National Laboratory using a bending magnet source at X-ray Science Division (XSD) Beamline 20 (20-BM-B). The ionization chambers were optimized for the maximum current with linear response (*ca.* 10^{10} photons detected s^{-1}). The Rh K-edge (23.220 keV) and Re L_{III}-edge (10.350 keV) were probed to obtain the extended X-ray absorption fine structure (EXAFS) and X-ray absorption near-edge structure (XANES). All spectra were obtained in transmission mode. A Pt foil (K-edge: 24.35 keV) was used to align the monochromator before Rh K-edge measurements. A Ga foil (K-edge: 10.37 keV) was used to align the monochromator before Re L_{III}-edge measurements. The XANES data had a resolution of 0.14 eV.

The catalyst samples were pressed into a cylindrical sample holder consisting of six wells, each forming a self-supporting wafer. The catalyst amount used was calculated to give an absorbance (μx) of approximately 1.0 for the Rh K-edge measurements and 0.3–0.4 for the Re L_{III}-edge measurements (the latter due to high white line absorbance). The catalysts were reduced in a continuous-flow reactor, which consisted of the six-well sample holder placed in the center of a quartz tube (2.54 cm OD, 25.4 cm length) sealed with Kapton windows by two Ultra-Torr fittings. Ball valves were welded to each Ultra-Torr fitting and served as the gas inlet and outlet. An internal K-type thermocouple (Omega) was placed against the catalyst sample holder to monitor the temperature. The catalysts were reduced in flowing 3.5 vol% H_2 in He (100 mL min^{-1}) while heating to 473 K at 4 K min^{-1} and holding for 15 min. After the reactor cooled to room temperature, the quartz tube was purged with flowing He for 5 min, sealed by closing the ball valves, and transported to the beamline hutch for XAS analysis. Another set of scans was obtained for each catalyst in its reduced and passivated form.

2.3.7. XAS data analysis. The normalized, energy calibrated Rh K-edge and Re L_{III}-edge XANES spectra were obtained by standard methods using Athena XAS analysis software. The edge energy was determined from the maximum in the first peak of the first derivative of the XANES. XANES fits were determined as a linear combination of the reference spectra. Theoretical phase and amplitude functions were obtained from FEFF6 simulations of crystallographic information files (CIF) for the Re metal (space group: *P*63/*mmc*), ReO_2 (*Pbcn*), the Rh metal (*Fm*$\bar{3}$*m*), and Rh_2O_3 (*Pbca*). Rh–Re and Re–Rh coordination was calculated with FEFF6 using two-atom calculation with an interatomic distance of 2.63 Å. An amplitude reduction factor (S_0^2) of 0.92 was used for both Re and Rh. As standard foils were unable to fit in the beamline, this value had to be assumed based on previous studies.[28] This value should be close to the actual S_0^2 under our conditions, but a small error in absolute (not relative) coordination numbers may have been introduced. Standard procedures using Artemis software were employed to fit the XAS data to obtain coordination numbers. The EXAFS parameters were obtained by a least squares fit in *R*-space of the k^2-weighted Fourier transform (FT) data.

2.3.8. Scanning transmission electron microscopy (STEM). STEM imaging was performed using a Titan STEM (FEI) with Cs aberration correction operated at 200 kV in high-angle annular dark field (HAADF) mode. Energy dispersive X-ray spectra (EDS) were collected using the same microscope with an EDAX SiLi detector. Before imaging, the catalyst samples were reduced in H_2 at 723 K, then cooled to room temperature and sealed in an H_2 atmosphere in a Schlenk tube. To avoid leaching of the oxophilic Re into the solution,[29] the tubes were opened in an Ar atmosphere to avoid contact with air. The samples were suspended in ethanol and then dropped on a carbon-coated copper grid. The STEM grids were plasma cleaned before being loaded in the microscope.

3. Results and discussion

3.1. Hydrogenolysis of THP-2M

3.1.1. Catalytic performance of RhRe/VXC. The THP-2M hydrogenolysis conversion as well as the 1,6-HDO selectivity obtained over a RhRe/VXC catalyst in a continuous flow reactor is displayed in Fig. 1 as a function of time-on-stream. The conversion of THP-2M decreased from 60% to 30% within the first 30 hours of reaction, but remained stable at longer times on stream. The activity decrease may have been caused by metal migration or sintering during the initial course of reaction. 1,6-HDO was formed with >80% selectivity at times on stream above 20 h. By-products included other C6 compounds, including 1-hexanol (1% selectivity) and 2-methyltetrahydropyran (2-MTHP, 1% selectivity); and small quantities of C–C cracking products, including 1-pentanol (3% selectivity) and tetrahydropyran (THP, 1% selectivity). Small amounts of methane (2% selectivity) were observed in the gas effluent from the reactor.

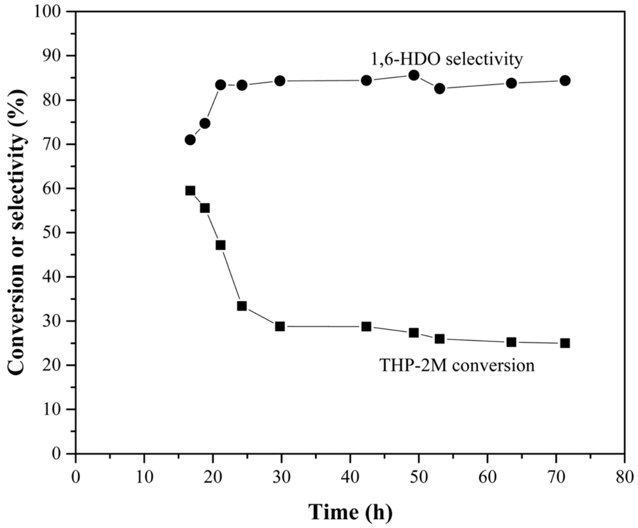

Fig. 1 Hydrogenolysis of THP-2M in a fixed bed reactor. (■) Conversion of THP-2M and (●) selectivity to 1,6-HDO. Reaction conditions: 5% aq. THP-2M feedstock, catalyst: RhRe/VXC, WHSV = 1.44 h^{-1}, 393 K, 40 bar H_2.

Fig. 2 shows the time on stream performance of the same RhRe/VXC catalyst for the hydrogenolysis of THP-2M in the 50 mL batch reaction. After 74 h of reaction time, the THP-2M conversion reached 72%. The selectivity of 1,6-HDO was >90% over the course of the reaction. Small quantities of 1-hexanol, 2-MTHP, 1-pentanol, and THP were also formed.

3.1.2. Comparison of RhRe/VXC with RhRe/NDC. We synthesized the RhRe/NDC catalyst with the same loadings of Rh and Re as in RhRe/VXC. Table 1 and Fig. 2 compare their activities in the batch reaction experiments. The RhRe/VXC catalyst displayed hydrogenolysis rates almost 2 orders of magnitude higher than those of RhRe/NDC. The main product of THP-2M hydrogenolysis over RhRe/NDC was 2-propanol, with no 1,6-HDO produced during the 15 h reaction. Even up to 23 h time of reaction, RhRe/NDC exhibited very low activity relative to RhRe/VXC (Fig. 2)

3.1.3. Effect of catalyst pretreatment after catalyst synthesis. Table 2 shows the effect of the reduction temperature during catalyst synthesis on the performance of the RhRe/VXC catalyst in batch reactions. During the synthesis, RhRe/

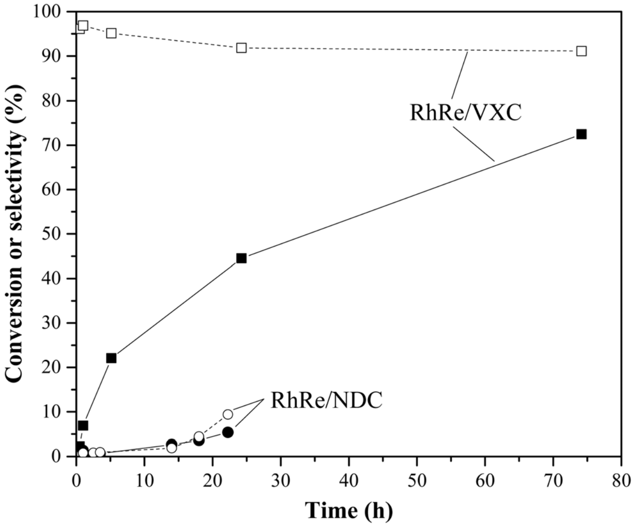

Fig. 2 Hydrogenolysis of THP-2M in a batch reactor with RhRe/NDC and RhRe/VXC. THP-2M conversion (●) and 1,6-HDO selectivity (○) with RhRe/NDC. THP-2M conversion (■) and 1,6-HDO selectivity (□) with RhRe/VXC. Reaction conditions: 5% aq. THP-2M feedstock (initial reaction volume = 50 mL), mass ratio of catalyst : feedstock = 1 : 7, 393 K, 40 bar H_2.

Table 1 Hydrogenolysis of THP-2M over bifunctional RhRe catalysts supported on NDC and VXC supports. Reaction conditions: 5 wt% aqueous feedstock solution (25 mL), mass ratio of catalyst : feedstock = 1 : 7, 393 K, 40 bar H_2

Catalyst	Time (h)	Conversion (%)	Product selectivity (%) 1,6-HDO	1-Hexanol	2-MTHP	1-Pentanol	Others (C1–C4)	Specific rate (μmol g^{-1} min^{-1})
RhRe/VXC	4	33	91	3	3	1	3	76
RhRe/NDC	15.2	1	0	0	0	0	4	1

Table 2 Effect of pretreatment temperature on the performance of the RhRe/VXC catalyst for THP-2M hydrogenolysis

Pretreatment reduction temperature (K)	Time (h)	Conversion (%)	Product selectivity (%) 1,6-HDO	1-Hexanol	2-MTHP	1-Pentanol	Others	Specific rate (μmol g^{-1} min^{-1})
723	4	33	91	3	3	1	3	76
523[a]	4	40	78	3	4	2	2	102

[a] The carbon balance for the catalyst reduced at 523 K is only 94% (unlike ~100% for all experiments when the catalyst was reduced at 723 K). Because of the 94% carbon balance, the selectivities do not add up to ~100%.

VXC was reduced at one of two reduction temperatures (523 K and 723 K) followed by passivation and then, prior to reaction, it was reduced a second time at 473 K. The hydrogenolysis reaction rate over the catalyst with the pretreatment reduction temperature of 523 K was 30% higher than that of the catalyst initially reduced at 723 K (see Table 2). Chia *et al.* studied the effect of reduction temperature on the activity of RhRe/VXC catalysts by changing the final reduction temperature (the reduction temperature during the catalyst synthesis was the same for all catalysts, 723 K) and reported a similar trend with the rate of reaction increasing as the reduction temperature decreased from 723 K to 393 K.[5] Falcone *et al.* reported a greater extent of Re segregation to the core of a PtRe/VXC catalyst when they increased the reduction temperature from 393 K to 473 K.[6] This link between higher reduction temperature and segregation of the catalysts' metal components is significant; one of the main findings of this work is that segregated RhRe/C is less active than well mixed RhRe/C. We also note that, while less active, the catalyst reduced at higher temperature displayed a higher selectivity to 1,6-HDO.

3.2. Characterization of the carbon supports

3.2.1. Physisorption. Table 3 compares the physical properties of the two carbon supports used in this study. NDC is an activated carbon support; it has a BET surface area three times higher than that of VXC support. The NDC support also has three times higher micropore area than the VXC support (see the ESI† Fig. S1). NDC's pore size distribution is relatively narrow, with 40 Å (average) mesopores (Fig. S2†). Fig. 3 shows the water adsorption isotherms for the NDC and VXC supports. The water uptake by NDC at lower relative pressures indicates the presence of oxygen-containing functional groups on its surface.[30] The water adsorption capacity of VXC was found to be 1.2 mmol g^{-1} compared to 17.5 mmol g^{-1} for NDC, indicating that the VXC support is hydrophobic relative to NDC.

Table 3 Physical properties of the two carbon supports

Property	NDC	VXC
BET surface area (m^2 g^{-1})	671	237
t-Plot micropore area (m^2 g^{-1})	299	81
Water adsorption capacity[a] (mmol g^{-1})	17.5	1.2

[a] Reported from the water adsorption isotherms at P/P_o = 0.82.

3.2.2. Characterization of the carbon supports by XPS, Raman, and DRIFTS. Table 4 compares the atomic compositions of the NDC and VXC support surfaces measured by XPS. The biggest difference between the two carbons is their oxygen content; NDC carbon has 20 times more surface oxygen than VXC carbon. The higher concentration of oxygen on the surface of NDC is most likely due to acid treatments during the carbon activation process.[23,31] This XPS result is consistent with the higher water uptake by the NDC support. The higher oxygen population of the NDC surface may provide

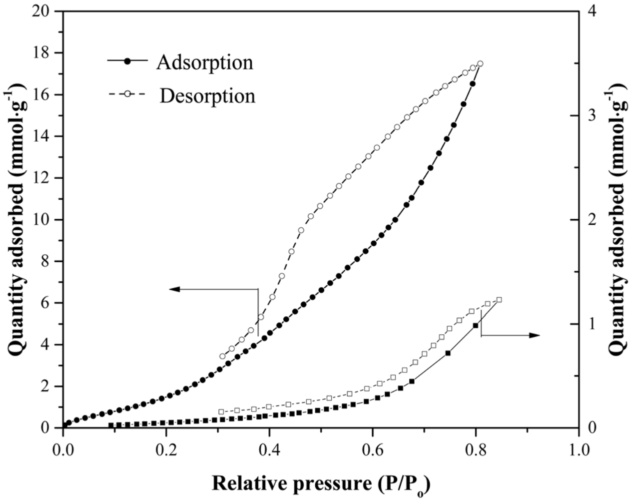

Fig. 3 Water adsorption isotherms for (●) NDC and (■) VXC supports.

sites that can preferentially interact with one of the two metal precursors.

Fig. 4 shows the raw and fitted DRIFTS spectra for the two carbon supports. Table 5 summarizes the results of deconvolution of the DRIFTS spectra. A relative abundance value was defined for different surface functional groups relative to the C═C stretch, which is the only signal due to a non-oxygenated bond that appears in both carbons. However, because the carbons are likely to have different C═C stretch intensities, absolute populations of the various surface functional groups across the samples cannot be estimated accurately. Despite this uncertainty, we note that the surface of NDC clearly contains a variety of oxygen-containing functionalities, which are either completely absent or present in smaller amounts on the surface of the VXC support. The Raman spectra of the carbons (Fig. S3†) are typical of graphitic materials.

3.3. Characterization of bifunctional catalysts

3.3.1. CO chemisorption. Table 6 summarizes the CO chemisorption results for the catalysts used in this study. Monometallic Rh/NDC displayed a higher CO/Rh ratio than Rh/VXC, indicative of a higher extent of Rh dispersion on NDC. After addition of Re to the Rh/VXC catalyst, the CO uptake decreased from 130 μmol g^{-1} to 76 μmol g^{-1}. This finding is consistent with other reports of reduction in CO-accessible metal sites upon addition of oxophilic promoters, including addition of Re to Rh.[4,8] In contrast, the CO uptake slightly increased when Re was added to the monometallic Rh/NDC catalyst.

3.3.2. XAS analysis. Table 7 provides a summary of the Rh K-edge and Re L_{III}-edge XANES fits. The Re L_{III}-edge XANES spectra of Re foil, ReO_2, Re_2O_7, Re/NDC, and Re/VXC are shown in Fig. 5a. The XANES data show that the extent of Rh reduction was similar for RhRe/NDC and RhRe/VXC at 473 K (∼90% and ∼84% reduced, respectively). Monometallic Re in Re/NDC and Re/VXC remains fully oxidized even after reduction pretreatment at 473 K. However, Re is reduced in both bimetallic catalysts at 473 K. This is consistent with the report of Chia *et al.*, who showed that (1) temperatures higher than 723 K are required to reduce Re to a metallic state and (2) the presence of metallic Rh promotes the reduction of Re.[5] The Re L_{III}-edge XANES spectra of RhRe/VXC and RhRe/NDC (Fig. 5b) show that, respectively, 83% and 87% of the Re is reduced in these catalysts after reduction at 473 K.

The values of parameters from the *R*-space fits of the Rh K-edge and Re L_{III}-edge EXAFS spectra for Rh and Re standards, RhRe/VXC, and RhRe/NDC catalysts are reported in Table 8. The Cowley short-range order parameter (α) has been used to estimate the degree of segregation of each species in bimetallic materials.[32,33] A Cowley parameter value $-1 \leq \alpha < 0$ suggests that clustering of atoms is not favored, while $0 < \alpha \leq 1$ suggests component segregation.[33] Using the

Table 4 Surface compositions of the two carbon supports as obtained by XPS

	Surface composition (mol%)					
Carbon	C	O	S	Si	Al	Na
NDC	88.8	8.8	0	1.9	0.3	0.2
VXC	99.4	0.4	0.2	0	0	0

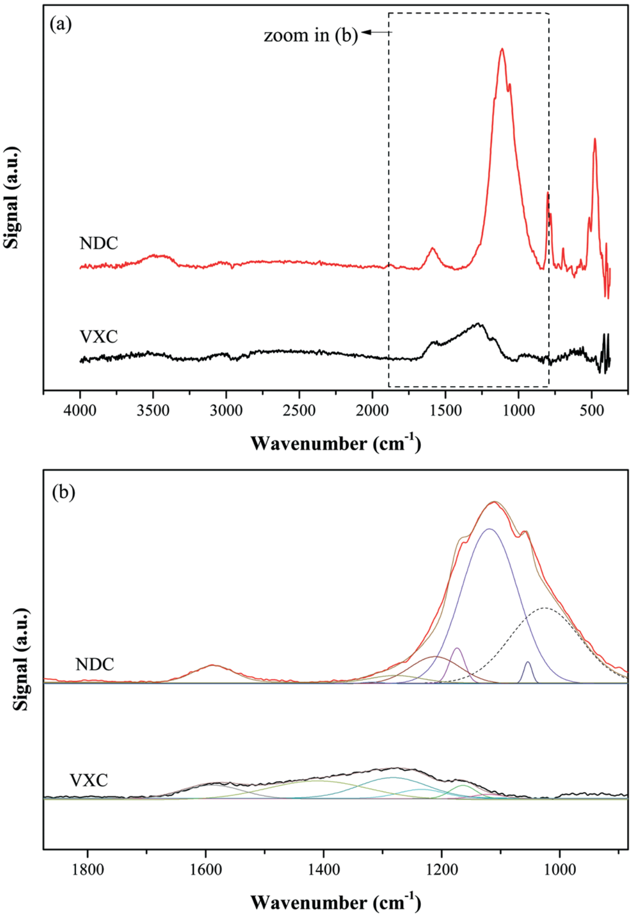

Fig. 4 DRIFTS spectra for NDC and VXC supports: (a) experimental DRIFTS signals (b) fitted signals.

Table 5 Relative abundance of different surface functionalities on the carbon supports based on DRIFTS. The abundance shown is relative to the area of the C═C stretch

Band position (cm^{-1})	Assignment	Relative abundance	
		NDC	VXC
477	C–CO deformation of cyclic ketone	3.407	0
792	C–O–C stretch of aromatic cyclic anhydride or O–H bend of carboxylic acid	1.692	0
1023	Acid anhydride C–O–C stretch	7.917	0
1055	Phenol O–H bend	0.265	0
1119	Ether C–O–C stretch	13.07	0.165
1173	Phenol C–OH stretch	0.805	0.421
1215	Lactone C═O stretch	2.051	0.512
1280	Carboxylic acid C═O stretch	0.558	1.787
1350	Carboxyl carbonate C═O stretch	0.049	2.406
1586	C═C stretch (conjugated aromatic)	1	1
3473	O–H stretch of water or carboxylic acid	1.986	0.959

Table 6 Results of CO pulse chemisorption characterization of the catalysts used in this study

Catalyst	Rh loading (wt%)	Re loading (wt%)	Rh : Re (mol : mol)	Irreversible CO uptake (μmol g^{-1})	CO : Rh (mol : mol)
Rh/NDC	4	—	—	204	0.51
RhRe/NDC	3.9	3.6	1 : 0.5	232	0.60
Rh/VXC	4	—	—	130	0.32
RhRe/VXC	4	3.6	1 : 0.5	76	0.19

metal–metal coordination values from Table 8, the Cowley parameters for Rh in RhRe/NDC and RhRe/VXC were found to be −0.31 and −0.07, respectively. The more negative value for RhRe/NDC suggests less clustering of Rh, owing to smaller Rh particles as also suggested by STEM–EDS analysis in section 3.3.3. The Cowley parameter for Re in RhRe/NDC is 0.08, *versus* a value of 0.12 for RhRe/VXC; the difference is well within the error associated with Cowley parameter analysis. This result suggests that the Re is more segregated than the Rh in both RhRe/NDC and RhRe/VXC (positive α values) and even forms some monometallic Re particles as seen from STEM–EDS analysis (see section 3.2.3). It is important to note that over-interpretation based on Cowley parameters should be avoided, as the analysis was originally developed for bulk alloys rather than catalyst nanoparticles.[32]

Several previous studies have used XAS to characterize supported bimetallic RhRe catalysts in order to gain understanding about the active site for hydrogenolysis.[5,34–36] We would like to note that the use of bulk XAS data to accurately represent local coordinations in nanoparticles requires that the catalyst nanoparticles have a uniform composition throughout the catalyst. This is not the case for RhRe/NDC which shows segregation of Re species on the surface (see section 3.3.3).

3.3.3. STEM and EDS. The STEM images of RhRe/NDC and RhRe VXC are shown in Fig. 6. For each sample, approximately 800 particles were measured to estimate the average particle sizes. The average particle sizes of RhRe/NDC and RhRe/VXC were 1.61 ± 0.61 nm and 1.98 ± 0.73 nm, respectively; particles on the NDC support were, on average, larger, but the difference is not statistically significant. The compositions of the metal particles were measured by spot beam EDS analysis of over 50 particles in each sample. For greater stability and to decrease the extent of beam damage during composition analysis, the particles chosen for analysis are, on average, larger than the general population. General population and EDS sample particle sizes are compared in Table 9. Fig. 7 compares the number distribution of particle compositions in the two samples. Both samples contain measurable populations of monometallic particles. Re-only particles are more common than Rh-only particles, especially in the NDC-supported catalyst; this result is consistent with the Cowley analysis of the EXAFS data. Aside from the monometallic "tails," the compositions of the particles on the VXC support exhibit an approximately normal distribution, with an average Rh : Re atomic ratio of 1.0 : 0.58, which is very close to both the ratio determined by ICP analysis (1.0 : 0.51) and the design ratio (1.0 : 0.50) (see Table 9). In contrast, the composition distribution of the NDC-supported metals is "flatter". More important, however, is that the average Rh : Re EDS ratio of the NDC-supported catalyst is 1.0 : 1.58, which is significantly different from both its ICP and design ratios. The difference suggests that EDS analysis of the NDC-supported material does not detect all of the sample's Rh content. It is likely that particles on the NDC surface that are too small to be detected in the STEM, below *ca.* 1 nm, have large relative Rh contents.[29] Overall, the STEM/EDS characterization suggests differences in metal distribution on the surfaces of the two carbons. Rh and Re appear to be more uniformly distributed across particles of different sizes on the VXC surface than on NDC. On NDC, there is evidence of preferential location of Rh in very small particles, leaving larger particles enriched in Re.

Table 7 Fits of Rh K-edge and Re L_{III}-edge XANES for the monometallic Re/C and RhRe/C catalysts prepared using two different carbon supports

Catalyst	Treatment/scan conditions	Edge energy (keV)	XANES fit		
Rh edge		23.22		Rh(III)	Rh(0)
RhRe/NDC	No/He RT			0.908	0.092
RhRe/VXC	No/He RT			0.550	0.450
RhRe/NDC	H_2 473 K/He RT			0.12	0.88
RhRe/VXC	H_2 473 K/He RT			0.16	0.84
Re edge		10.53	Re(IV)	Re(VII)	Re(0)
Re/NDC	No/He RT		0.630	0.370	—
Re/VXC	No/He RT		0.468	0.532	—
Re/NDC	H_2 473 K/He RT		0.702	0.298	—
Re/VXC	H_2 473 K/He RT		0.642	0.358	—
RhRe/NDC	No/He RT		0.322	0.656	0.022
RhRe/VXC	No/He RT		0.807	—	0.193
RhRe/NDC	H_2 473 K/He RT		0.13	—	0.87
RhRe/VXC	H_2 473 K/He RT		0.17	—	0.83

4. Discussion

Bimetallic RhRe/C catalysts with identical (wt%) metal loadings, but prepared on two different carbon supports, NDC and VXC, displayed activities for hydrogenolysis of THP-2M that differed by two orders of magnitude.

Characterization of the carbon supports and the bimetallic catalysts provide insight into how different catalytic structures, with different activities for the hydrogenolysis reaction, may evolve on the surfaces of the two carbons during catalyst preparation. To form bimetallic sites that are active for THP-

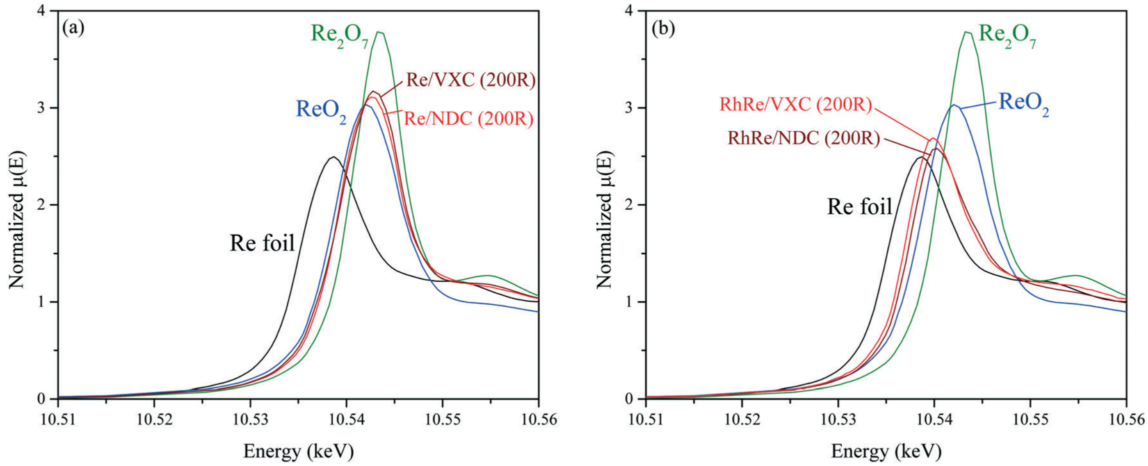

Fig. 5 Re L_{III}-edge XANES spectra (10.52–10.56 keV) of (a) monometallic Re/NDC and Re/VXC reduced at 473 K and (b) RhRe/NDC and RhRe/VXC reduced at 473 K. The spectra were acquired under *in situ* conditions.

Table 8 Fit of Rh K-edge and Re L_{III}-edge EXAFS for the RhRe/C catalysts prepared using two different carbon supports

Catalyst	Treatment/scan conditions	Absorber-backscatterer	N	R (Å)	$\Delta\sigma^2$ ($\times 10^3$ Å^2)	ΔE_o (eV)
Rh edge						
Rh foil	—	Rh–Rh	12.0	2.72		
RhRe/NDC	No/He RT	Rh–Rh	0.2	2.72	3.5	4.8
		Rh–Re	—	—	—	—
		Rh–O	3.6	—	2.7	6
RhRe/VXC	No/He RT	Rh–Rh	2.3	2.72	3.5	−5.4
		Rh–Re	1.5	2.63	2.0	3.6
		Rh–O	3.4	—	7.7	
RhRe/NDC	H_2 473 K/He RT	Rh–Rh	4.8	2.68	2.0	0.6
		Rh–Re	3.7	2.63	2.0	−14.0
		Rh–O	0.6	2.05	1.0	−1.9
RhRe/VXC	H_2 473 K/He RT	Rh–Rh	6.5	2.68	2.0	4.4
		Rh–Re	3.6	2.63	2.0	−4.4
		Rh–O	—	—	—	—
Re edge						
Re foil	—	Re–Re	12.0	2.75		
RhRe/NDC	H_2 473 K/He RT	Re–O	0.4	1.75	1.0	9.7
		Re–Re	3.5	2.66	2.0	−9.3
		Re–Rh	5.6	2.63	2.0	2.7
RhRe/VXC	H_2 473 K/He RT	Re–O	0.2	1.75	1.0	9.3
		Re–Re	4.4	2.66	2.0	−3.8
		Re–Rh	6.3	2.63	2.0	−0.4

2M hydrogenolysis, Rh must (1) be accessible to the reactant and (2) be in close proximity to Re sites. In the impregnation steps, Rh and Re precursors are distributed, presumably statistically, across the carbon surfaces. At a constant metal loading, the areal densities of the precursors are significantly lower on the NDC surface, simply because of its higher surface area. When the precursors decompose in the reduction step, their metal components must migrate across the carbon surfaces to assemble in their final configurations. Formation of necessary bimetallic structures on the NDC surface may be hindered by two factors. First, because of lower areal densities, metal atoms must travel longer distances on the NDC surface to combine into large particles. Second, and perhaps more important, is that interactions of one of the metals with surface oxygen functionalities may restrict its mobility. In our case, Rh may become anchored on the NDC surface in this manner, while Re does not. Hence, relatively few large Rh-containing particles—ones that could be characterized for composition by EDS—form; much of the catalyst's Rh content exists in the form of tiny Rh-rich particles (and, therefore is as accessible in CO chemisorption as monometallic Rh/NDC). Mobile Re may be, on the other hand, free to associate with the few larger Rh-containing particles that do form to create bimetal particles that are rich in surface Re—so rich that the particle surfaces expose few of the bimetallic sites required for successful reaction. In contrast, on VXC, the O-free low area surface facilitates assembly of a distribution of bimetallic particles with an average surface Rh : Re ratio near the design target, and is therefore a catalyst that is active for the hydrogenolysis reaction.

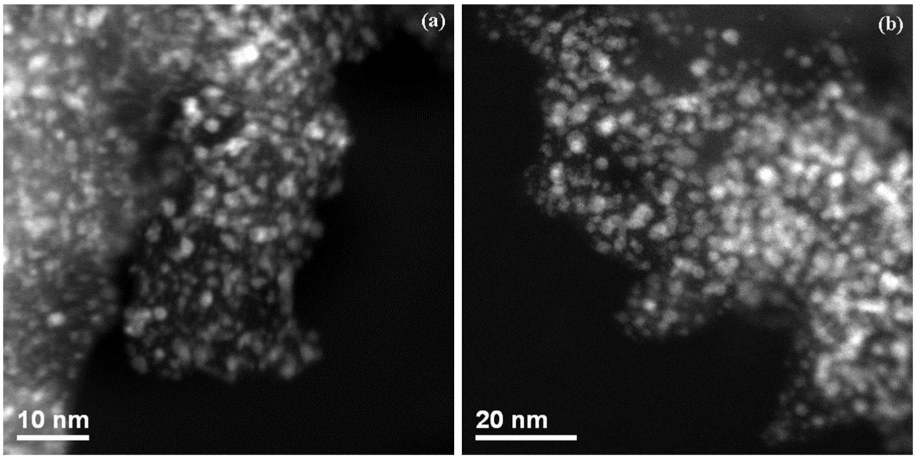

Fig. 6 STEM images of RhRe catalysts supported on the two carbon supports: (a) RhRe/NDC and (b) RhRe/VXC.

Table 9 Catalyst particle size and Re composition from ICP and STEM–EDS

Catalyst	Rh : Re (mol : mol) theoretical	Rh : Re (mol : mol) ICP	Rh : Re (mol : mol) EDS	Average particle size[a] (nm)	Average particle size used for EDS (nm)
RhRe/NDC	1 : 0.5	1 : 0.55	1 : 1.58	1.61 ± 0.61	2.53 ± 0.84
RhRe/VXC	1 : 0.5	1 : 0.51	1 : 0.58	1.98 ± 0.73	4.12 ± 1.09

[a] Histogram for the particle size distribution is available in the ESI (Fig. S4).

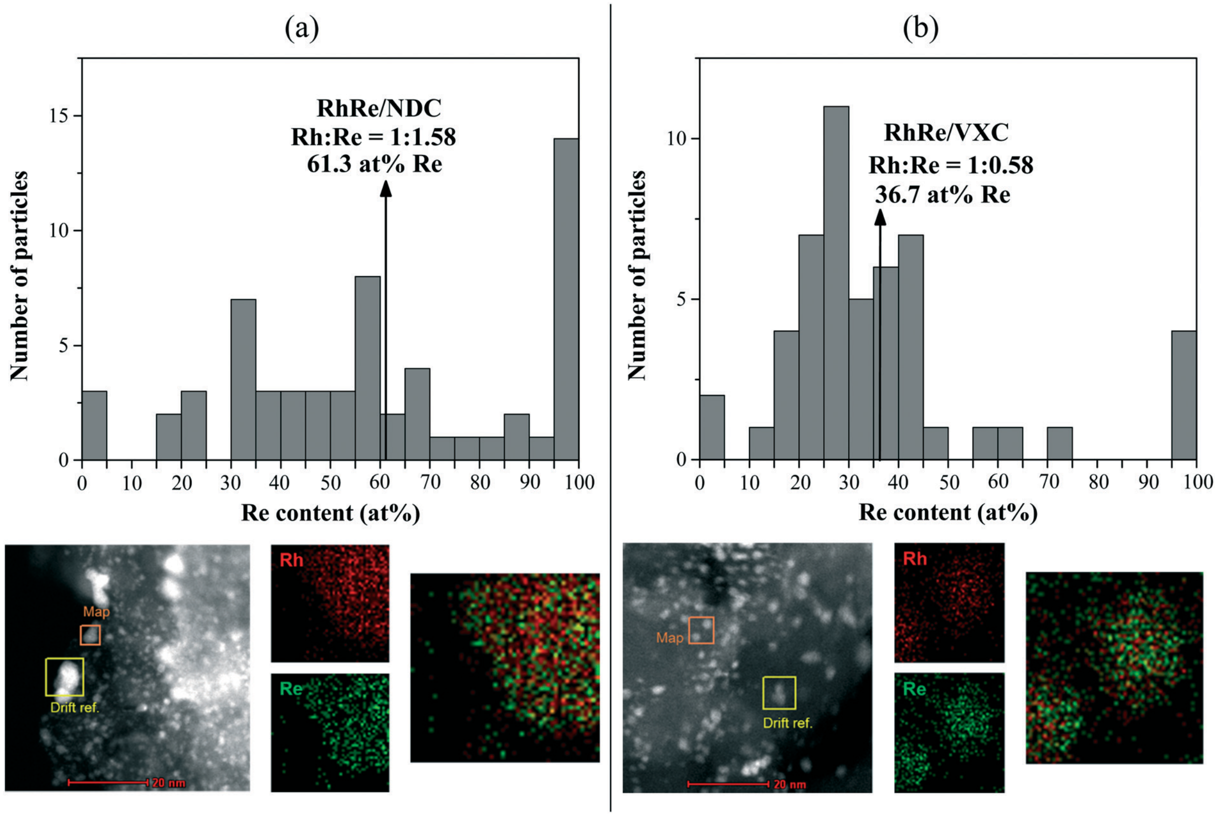

Fig. 7 Composition distribution for the catalysts, obtained by EDS spot beam analysis. (a) RhRe/NDC – average composition 61.3 atomic% Re determined over 59 particles. (b) RhRe/VXC – average composition 36.7 atomic% Re determined over 52 particles. Both catalysts have a theoretical composition of 33.3 atomic% Re.

5. Conclusion

Bimetallic RhRe catalysts with 4 wt% Rh and an Rh : Re atomic ratio of 1.0 : 0.5 were prepared on Vulcan XC-72 (VXC) and Norit Darco 12X40 (NDC) carbon supports. Under constant reaction conditions, the VXC supported catalyst displayed hydrogenolysis rates over two orders-of-magnitude higher than those of the NDC-supported catalyst. The activity differences are linked to differences in the metal distribution on the carbon surfaces. Characterization of the catalysts by STEM–EDS suggests that the bimetallic particles on the VXC surface are relatively uniform in composition, with most near the design target ratio of Rh : Re = 1.0 : 0.5. In contrast, NDC-supported particles appear to exist as either tiny Rh-rich particles or larger bimetallic particles with a higher than design Re content – both being inactive for the reaction. Metal distributions are, in turn, likely related to the properties of the carbons on which they are supported. NDC has ∼3 times higher surface area than VXC (BET surface area of 671 m^2 g^{-1} *vs.* 237 m^2 g^{-1}) and has 20 times higher surface oxygen content; both of these characteristics may restrict the movement of metals and their precursors across the NDC surface and their ability to assemble into the forms required for an active catalyst.

Acknowledgements

This material is based upon work supported by the Department of Energy, Office of Energy Efficiency and Renewable Energy (EERE), under Award Number DE-EE0006878. Sector 20 facilities at the Advanced Photon Source and research at these facilities are supported by the US Department of Energy – Basic Energy Sciences, the Canadian Light Source and its funding partners, and the Advanced Photon Source. Use of the Advanced Photon Source, an Office of Science User Facility operated for the U.S. Department of Energy (DOE) Office of Science by Argonne National Laboratory, was supported by the U.S. DOE under Contract No. DE-AC02-06CH11357. The authors gratefully acknowledge support of this research by NSF through the use of instrumentation at the University of Wisconsin Materials Research Science and Engineering Center (DMR-1121288) and the University of Wisconsin-Madison Nanoscale Science and Engineering Center (DMR-0832760). The authors also acknowledge the use of instrumentation supported by the University of Wisconsin Materials Science Center. Xiaoli Chen acknowledges financial support provided by the China Scholarship Council (CSC) for Overseas Studies.

References

1 Y. Nakagawa, M. Tamura and K. Tomishige, *ACS Catal.*, 2013, **3**, 2655–2668.

2 T. Buntara, S. Noel, P. Phua, I. Melián-Cabrera, J. Vries and H. Heeres, *Top. Catal.*, 2012, **55**, 612–619.

3 T. Buntara, S. Noel, P. H. Phua, I. Melián-Cabrera, J. G. de Vries and H. J. Heeres, *Angew. Chem., Int. Ed.*, 2011, **50**, 7083–7087.

4 M. Chia, Y. J. Pagán-Torres, D. Hibbitts, Q. Tan, H. N. Pham, A. K. Datye, M. Neurock, R. J. Davis and J. A. Dumesic, *J. Am. Chem. Soc.*, 2011, **133**, 12675–12689.

5 M. Chia, B. J. O'Neill, R. Alamillo, P. J. Dietrich, F. H. Ribeiro, J. T. Miller and J. A. Dumesic, *J. Catal.*, 2013, **308**, 226–236.

6 D. D. Falcone, J. H. Hack, A. Y. Klyushin, A. Knop-Gericke, R. Schlögl and R. J. Davis, *ACS Catal.*, 2015, **5**, 5679–5695.

7 O. M. Daniel, A. DeLaRiva, E. L. Kunkes, A. K. Datye, J. A. Dumesic and R. J. Davis, *ChemCatChem*, 2010, **2**, 1107–1114.

8 K. Chen, S. Koso, T. Kubota, Y. Nakagawa and K. Tomishige, *ChemCatChem*, 2010, **2**, 547–555.

9 S. Koso, Y. Nakagawa and K. Tomishige, *J. Catal.*, 2011, **280**, 221–229.

10 S. Koso, H. Watanabe, K. Okumura, Y. Nakagawa and K. Tomishige, *Appl. Catal., B*, 2012, **111–112**, 27–37.

11 K. Chen, K. Mori, H. Watanabe, Y. Nakagawa and K. Tomishige, *J. Catal.*, 2012, **294**, 171–183.

12 S. Koso, I. Furikado, A. Shimao, T. Miyazawa, K. Kunimori and K. Tomishige, *Chem. Commun.*, 2009, 2035–2037.

13 E. Auer, A. Freund, J. Pietsch and T. Tacke, *Appl. Catal., A*, 1998, **173**, 259–271.

14 E. Furimsky and J. J. Spivey, *Carbons and Carbon Supported Catalysts in Hydroprocessing*, The Royal Society of Chemistry, 2008.

15 Y. T. Kim, J. A. Dumesic and G. W. Huber, *J. Catal.*, 2013, **304**, 72–85.

16 P. J. Dietrich, R. J. Lobo-Lapidus, T. Wu, A. Sumer, M. C. Akatay, B. R. Fingland, N. Guo, J. A. Dumesic, C. L. Marshall, E. Stach, J. Jellinek, W. N. Delgass, F. H. Ribeiro and J. T. Miller, *Top. Catal.*, 2012, **55**, 53–69.

17 H. J. Park, H.-D. Kim, T.-W. Kim, K.-E. Jeong, H.-J. Chae, S.-Y. Jeong, Y.-M. Chung, Y.-K. Park and C.-U. Kim, *ChemSusChem*, 2012, **5**, 629–633.

18 X. Di, Z. Shao, C. Li, W. Li and C. Liang, *Catal. Sci. Technol.*, 2015, **5**, 2441–2448.

19 W. Brandl and G. Marginean, *Thin Solid Films*, 2004, **447–448**, 181–186.

20 F. Rodríguez-reinoso, *Carbon*, 1998, **36**, 159–175.

21 C. Moreno-Castilla, M. A. Ferro-Garcia, J. P. Joly, I. Bautista-Toledo, F. Carrasco-Marin and J. Rivera-Utrilla, *Langmuir*, 1995, **11**, 4386–4392.

22 S. Jin, Z. Xiao, X. Chen, L. Wang, J. Guo, M. Zhang and C. Liang, *Ind. Eng. Chem. Res.*, 2015, **54**, 2302–2310.

23 J. L. Figueiredo, M. F. R. Pereira, M. M. A. Freitas and J. J. M. Órfão, *Carbon*, 1999, **37**, 1379–1389.

24 A. Cabiac, T. Cacciaguerra, P. Trens, R. Durand, G. Delahay, A. Medevielle, D. Plée and B. Coq, *Appl. Catal., A*, 2008, **340**, 229–235.

25 M. Wojdyr, *J. Appl. Crystallogr.*, 2010, **43**, 1126–1128.

26 P. E. Fanning and M. A. Vannice, *Carbon*, 1993, **31**, 721–730.

27 J. Collins, T. Ngo, D. Qu and M. Foster, *Carbon*, 2013, **57**, 174–183.

28 R. J. Lobo-Lapidus and B. C. Gates, *Chem. – Eur. J.*, 2010, **16**, 11386–11398.

29 A. C. Alba-Rubio, C. Sener, S. H. Hakim, T. M. Gostanian and J. A. Dumesic, *ChemCatChem*, 2015, **7**, 3881–3886.
30 S. S. Barton, M. J. B. Evans and J. A. F. MacDonald, *Carbon*, 1991, **29**, 1099–1105.
31 C. Moreno-Castilla, M. V. López-Ramón and F. Carrasco-Marín, *Carbon*, 2000, **38**, 1995–2001.
32 J. M. Cowley, *Phys. Rev.*, 1965, **138**, A1384–A1389.
33 A. I. Frenkel, Q. Wang, S. I. Sanchez, M. W. Small and R. G. Nuzzo, *J. Chem. Phys.*, 2013, **138**, 064202.
34 Y. Shinmi, S. Koso, T. Kubota, Y. Nakagawa and K. Tomishige, *Appl. Catal., B*, 2010, **94**, 318–326.
35 Y. Amada, S. Koso, Y. Nakagawa and K. Tomishige, *ChemSusChem*, 2010, **3**, 728–736.
36 S. Koso, H. Watanabe, K. Okumura, Y. Nakagawa and K. Tomishige, *J. Phys. Chem. C*, 2012, **116**, 3079–3090.